Checkerboard bubble lattice formed by octuple-period quadruple-Q spin density waves

Satoru Hayami
Graduate School of Science, Hokkaido University, Sapporo 060-0810, Japan

(Received 18 July 2023; accepted 30 August 2023; published 8 September 2023)

We investigate multiple-Q instability on a square lattice at particular ordering wave vectors. We find that a superposition of quadruple-Q spin density waves, which are connected by fourfold rotational and mirror symmetries, gives rise to a checkerboard bubble lattice with a collinear spin texture as a result of the geometry among the constituent ordering wave vectors in the Brillouin zone. By performing the simulated annealing for a fundamental spin model, we show that such a checkerboard bubble lattice is stabilized under an infinitesimally small easy-axis two-spin anisotropic interaction and biquadratic interaction at zero field, while it is degenerate with an anisotropic double-Q state in the absence of the biquadratic interaction. The obtained multiple-Q structures have no intensities at high-harmonic wave vectors in contrast to other multiple-Q states, such as a magnetic skyrmion lattice. We also show that the checkerboard bubble lattice accompanies the charge density wave and exhibits a nearly flat-band dispersion in the electronic structure. Our results provide another route to realize exotic multiple-Q spin textures by focusing on the geometry and symmetry in terms of the wave vectors in momentum space.

DOI: 10.1103/PhysRevB.108.094415

I. INTRODUCTION

A multiple-Q state, which corresponds to a superposition of multiple spin density waves, has drawn considerable interest in condensed-matter physics, since it manifests itself in unusual magnetism but also in unconventional transport and cross-correlated response. One of the most familiar examples is a magnetic skyrmion lattice (SkL) [1–5], which ubiquitously appears in various lattice structures as a different multiple-Q superposition [6]: double-Q SkL in the tetragonal lattice structure [7–10], triple-Q SkL in the hexagonal lattice structure [2,3,11], and sextuple-Q SkL in the cubic lattice structure [12]. Another example is a magnetic hedgehog consisting of a periodic structure of monopole and antimonopole, which has been found as a consequence of the triple-Q or quadruple-Q spin density waves [13–18]. Moreover, various multiple-Q spin structures have been suggested/proposed from both theoretical and experimental studies, such as a vortex lattice [19–29], a chiral stripe [10,30–33], and a ripple state [34]. As a common feature in these multiple-Q states, the constituent ordering wave vectors are connected to each other by the rotational symmetry of the lattice structures.

We here investigate a different type of a multiple-Q state, which is characterized by a superposition of collinear spin textures, i.e., a bubble lattice [35–37]. Although such a bubble lattice does not exhibit a topological Hall effect in contrast to the SkL, it can be potentially applied to the growing field of antiferromagnetic/ferrimagnetic spintronics [38,39], since unconventional transport property is expected [40–42]. The isolated bubble and bubble lattices have been so far observed in easy-axis magnets [43], such as Fe/Rh atomic bilayers on the Ir(111) surface [44] hosting the triangular bubble lattice in Fig. 1(a) and $CeAuSb_2$ [45–48] hosting the square bubble lattice in Fig. 1(b); the former is described by the triple-Q collinear state, while the latter is described by the double-Q collinear state. Simultaneously, theoretical model calculations clarified various mechanisms of the bubble lattices, such as the competing exchange interaction with single-ion magnetic anisotropy [49], biquadratic interaction [50], high-harmonic wave-vector interaction [51], and thermal fluctuations [52].

In the present study, we propose a further intriguing bubble lattice in tetragonal magnets, which is characterized by a different multiple-Q superposition from the conventional bubble lattices. By focusing on the geometry and symmetry of the constituent ordering wave vectors, we find that a checkerboard bubble lattice is engineered on a square lattice by superposing quadruple-Q spin density waves with the octuple-period ordering wave vector, where we call it the quadruple-Q checkerboard bubble lattice (4Q CBL). We show that the 4Q CBL state is stabilized by taking into account an infinitesimally small easy-axis two-spin anisotropic interaction and positive biquadratic interaction by performing analytical and numerical analyses. In contrast to the conventional SkL and bubble lattice, the 4Q CBL state does not have the intensity at high-harmonic ordering wave vectors, which makes it difficult to distinguish it from a multidomain single-Q state by small-angle neutron scattering experiments. Instead, the real-space observation through spectroscopic-imaging scanning tunneling microscopy measurements [53] is one of the probes to identify the 4Q CBL state. Moreover, the 4Q CBL state exhibits a nearly flat-band structure in the strong-coupling regime. The present result indicates that multiple-Q superpositions can give rise to further exotic spin textures, which have not been observed in both theory and experiment, depending on the symmetry and geometry of the ordering wave vectors.

The organization of this paper is as follows. In Sec. II, we introduce a minimal spin model to induce the instability toward the 4Q CBL state. We also outline the numerical method based on the simulated annealing. Then, we show how to construct the 4Q CBL state by the multiple-Q superposition of

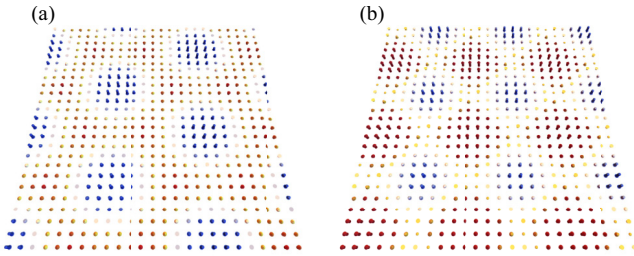

FIG. 1. Schematic pictures of (a) the triangular bubble lattice modulated by the triple-Q spin density waves and (b) the square bubble lattice modulated by the double-Q spin density waves. The arrows and the color represent the spin moments and their z direction component; the blue, red, and yellow stand for the up, down, and zero moments.

the octuple-period spin density waves in Sec. III. Furthermore, we discuss the stability region of the $4Q$ CBL state while changing an external magnetic field and easy-axis two-spin magnetic anisotropy. In Sec. IV, we discuss the charge density waves and the electronic band structure in the presence of the $4Q$ CBL spin texture. Section V summarizes this paper.

II. MODEL AND METHOD

We consider an effective spin model on a two-dimensional square lattice under the space group $P4/mmm$, which is obtained by tracing out the itinerant electron degree of freedom in the Kondo lattice model with the classical spin [54]. By supposing a weak Kondo coupling compared to the bandwidth of the itinerant electrons, one can obtain the following spin model based on the perturbative expansion [55]:

$$\mathcal{H} = -\sum_{\boldsymbol{q}} J_{\boldsymbol{q}} \sum_{\eta=x,y,z} (1+I^{\eta}) S^{\eta}_{\boldsymbol{q}} S^{\eta}_{-\boldsymbol{q}} + \sum_{\boldsymbol{q}} \frac{K_{\boldsymbol{q}}}{N} \left[\sum_{\eta=x,y,z} (1+I^{\eta}) S^{\eta}_{\boldsymbol{q}} S^{\eta}_{-\boldsymbol{q}} \right]^2 - H \sum_i S^z_i, \quad (1)$$

where $\boldsymbol{S}_{\boldsymbol{q}} = (S^x_{\boldsymbol{q}}, S^y_{\boldsymbol{q}}, S^z_{\boldsymbol{q}})$ is the $\boldsymbol{q}$ component of the spin moment, and $S^{\eta}_{\boldsymbol{q}}$ is related to the classical spin S^{η}_i at site i via the Fourier transformation. We fix the spin length at each site as $|\boldsymbol{S}_i| = 1$ and take the lattice constant as unity. The first term represents the bilinear exchange interaction, which is obtained from the lowest-order contribution in the perturbative expansion; the positive coupling constant $J_{\boldsymbol{q}} > 0$ is proportional to $J_{\rm K}^2$, where $J_{\rm K}$ stands for the Kondo coupling between the itinerant electron spin and the localized spin. This bilinear term is referred to as the Ruderman-Kittel-Kasuya-Yosida (RKKY) interaction [56–58]. We suppose the anisotropic form factor for the xy and z components as $I^z = -2I^x = -2I^y$, which originates from the relativistic spin-orbit coupling; $I^z > 0$ ($I^z < 0$) represents the easy-axis (easy-plane) anisotropy. Meanwhile, we ignore other magnetic anisotropy allowed from the symmetry of the square lattice, such as the bond-dependent magnetic anisotropy [59], since it does not affect the stability of the $4Q$ CBL state. The second term denotes the biquadratic interaction with the positive coupling constant $K_{\boldsymbol{q}} > 0$, which is derived from the second-lowest-order contribution in the perturbative expansion, i.e., $K_{\boldsymbol{q}} \propto J_{\rm K}^4$; N stands for the number of spins in the system. We neglect other multiple-spin interactions in the form of $(\boldsymbol{S}_{\boldsymbol{q}_1} \cdot \boldsymbol{S}_{\boldsymbol{q}_2})(\boldsymbol{S}_{\boldsymbol{q}_3} \cdot \boldsymbol{S}_{\boldsymbol{q}_4})$, with $\boldsymbol{q}_1 + \boldsymbol{q}_2 + \boldsymbol{q}_3 + \boldsymbol{q}_4 = \boldsymbol{0}$ by supposing the strong nesting of the Fermi surface in the band structure [55,60,61]. Since $K_{\boldsymbol{q}}$ corresponds to a higher-order term than $J_{\boldsymbol{q}}$ in terms of the Kondo coupling, we set $J_{\boldsymbol{q}} \gg K_{\boldsymbol{q}}$. The third term represents the Zeeman coupling in the presence of an external magnetic field along the out-of-plane direction.

We investigate the ground-state phase diagram of the model in Eq. (1) by changing the model parameters $J_{\boldsymbol{q}}$, $K_{\boldsymbol{q}}$, I^z, and H. Since we suppose $J_{\boldsymbol{q}} \gg K_{\boldsymbol{q}}$, the magnetic instability at zero temperature occurs at $\boldsymbol{q}^*$, satisfying $J_{\boldsymbol{q}^*} > J_{\boldsymbol{q}'}$ for $\boldsymbol{q}^* \neq \boldsymbol{q}'$; the circular (elliptical) spiral state with the spiral pitch $\boldsymbol{q}^*$ is expected for $I^z = 0$ ($I^z > 0$). It is noted that $\boldsymbol{q}'$ is determined by the electronic band structure and the chemical potential. In this situation, almost all of the wave vectors $\boldsymbol{q}'$ do not contribute to the energy, which indicates that the interactions in the $\boldsymbol{q}'$ channel are not relevant to determine the ground-state phase diagram. Similar attempts are done for investigating the square SkL, where several mechanisms have been clarified by analyzing minimal models, such as the Dzyaloshinskii-Moriya interaction [7,62,63], positive biquadratic interaction [64,65], magnetic anisotropy [66,67], dipolar interaction [68], and high-harmonic wave-vector interaction [65,69,70], and for modeling the materials hosting the SkL [71,72].

Then, we simplify the model by extracting the dominant $\boldsymbol{q}$ component of the interaction, which is given by

$$\mathcal{H} = -2J \sum_{\nu} \sum_{\eta=x,y,z} (1+I^{\eta}) S^{\eta}_{\boldsymbol{Q}_{\nu}} S^{\eta}_{-\boldsymbol{Q}_{\nu}} + 2\frac{K}{N} \sum_{\nu} \left[\sum_{\eta=x,y,z} (1+I^{\eta}) S^{\eta}_{\boldsymbol{Q}_{\nu}} S^{\eta}_{-\boldsymbol{Q}_{\nu}} \right]^2 - H \sum_i S^z_i. \quad (2)$$

We regard the interactions at $\boldsymbol{Q}_{\nu}$ for $\nu = 1$–4 as the dominant ones: $\boldsymbol{Q}_1 = (\pi/4, 3\pi/4)$, $\boldsymbol{Q}_2 = (3\pi/4, -\pi/4)$, $\boldsymbol{Q}_3 = (3\pi/4, \pi/4)$, and $\boldsymbol{Q}_4 = (-\pi/4, 3\pi/4)$, as schematically shown in Fig. 2. $\boldsymbol{Q}_1$–$\boldsymbol{Q}_4$ correspond to the octuple-period wave vectors. It is noted that $\boldsymbol{Q}_{\nu}$ are symmetry equivalent to each other; for example, $\boldsymbol{Q}_1$ is connected to $\boldsymbol{Q}_2$ by the fourfold rotational symmetry and $\boldsymbol{Q}_1$ is connected to $\boldsymbol{Q}_3$ by the mirror symmetry around the [110] direction. This means that the interaction constants $J_{\boldsymbol{q}}$ and $K_{\boldsymbol{q}}$ at $\boldsymbol{Q}_{\nu}$ are the same; we set $J \equiv J_{\boldsymbol{Q}_{\nu}}$ and $K \equiv K_{\boldsymbol{Q}_{\nu}}$ and choose J as the energy unit, i.e., $J = 1$. In other words, we consider the situation where the bare susceptibility of itinerant electrons shows maxima at $\boldsymbol{Q}_1$–$\boldsymbol{Q}_4$ by adjusting the model parameters and/or the chemical potential. As detailed in Sec. III A, the choice of octuple-period $\boldsymbol{Q}_{\nu}$ is important to induce the instability toward the $4Q$ CBL state. The prefactor 2 in the first and second terms represents the contribution from $-\boldsymbol{Q}_{\nu}$.

In the end, the ground-state phase diagram is numerically obtained by minimizing the energy of the model in Eq. (2) on the square lattice under the periodic boundary condition, where the system size is taken at $N = 16^2$; we confirmed that the obtained phase diagram is unchanged for different larger system sizes $N = 32^2$, 64^2, and 96^2. To unbiasedly determine the phase diagram, we adopt simulated annealing based on

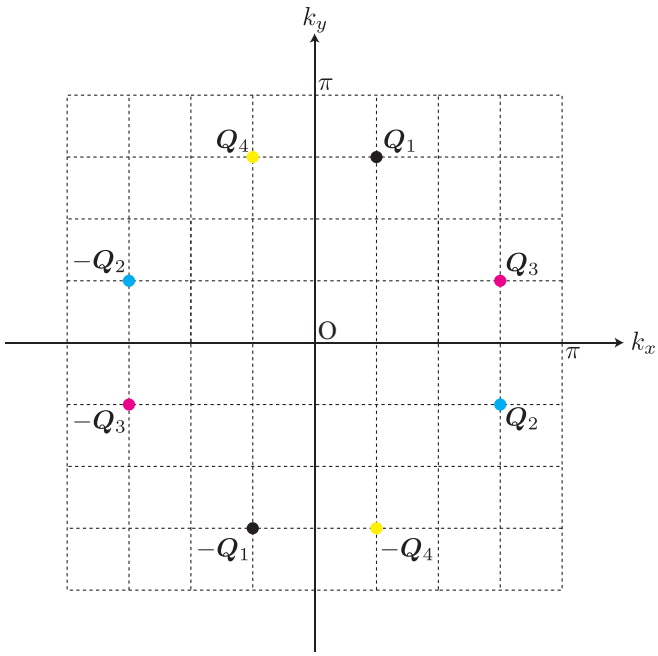

FIG. 2. Ordering wave vectors $\boldsymbol{Q}_1$–$\boldsymbol{Q}_4$ in the Brillouin zone with $-\pi < k_x \leqslant \pi$ and $-\pi < k_y \leqslant \pi$. $\boldsymbol{Q}_1$ and $\boldsymbol{Q}_2$ ($\boldsymbol{Q}_3$ and $\boldsymbol{Q}_4$) are connected by the fourfold rotational symmetry. $\boldsymbol{Q}_1$ and $\boldsymbol{Q}_3$ ($\boldsymbol{Q}_2$ and $-\boldsymbol{Q}_4$) are connected by the mirror symmetry along the [110] ([$\bar{1}$10]) axis. $\boldsymbol{Q}_1$ and $\boldsymbol{Q}_4$ ($\boldsymbol{Q}_2$ and $\boldsymbol{Q}_3$) are connected by the mirror symmetry along the k_y (k_x) axis.

the standard Metropolis local updates in real space in the following manner. First, we start from a random spin configuration at a high temperature $T_0 = 1.5$. By gradually reducing the temperature with a ratio of $T_{n+1} = 0.999\,999 T_n$ in each Monte Carlo sweep (T_n is the nth-step temperature), we try to avoid metastable spin configurations [73]. Once the temperature reaches the final temperature taken at $T_f = 0.0001$, we perform 10^5–10^6 Monte Carlo sweeps for measurements at the final temperature after 10^5–10^6 steps for thermalization. In order to determine the phase boundaries between different magnetic states, we also start from the spin patterns obtained at low temperatures by the above procedure; in this case, we start the simulations from $T_0 = 0.01$.

To distinguish the multiple-Q state from the single-Q state, we calculate the spin structure factor, which is given by

$$S_s^{\eta\eta}(\boldsymbol{q}) = \frac{1}{N}\sum_{i,j} S_i^\eta S_j^\eta e^{i\boldsymbol{q}\cdot(\boldsymbol{r}_i - \boldsymbol{r}_j)}, \tag{3}$$

for $\eta = x$, y, and z; $\boldsymbol{r}_i$ is the position vector at site i. We also compute the $\boldsymbol{Q}_\nu$ component of the magnetic moments as

$$m_{\boldsymbol{Q}_\nu}^\eta = \sqrt{\frac{S_s^{\eta\eta}(\boldsymbol{Q}_\nu)}{N}}. \tag{4}$$

For the in-plane spin component, we use the notation

$$m_{\boldsymbol{Q}_\nu}^{xy} = \sqrt{\frac{S_s^{xx}(\boldsymbol{Q}_\nu) + S_s^{yy}(\boldsymbol{Q}_\nu)}{N}}. \tag{5}$$

In addition, the net magnetization along the z direction is given by

$$M^z = \frac{1}{N}\sum_i S_i^z. \tag{6}$$

III. RESULTS

In this section, we discuss the stability of the $4Q$ CBL state. We show that the geometry and symmetry of the ordering wave vectors $\boldsymbol{Q}_1$–$\boldsymbol{Q}_4$ play an important role in inducing the multiple-Q superposition in Sec. III A; the energy for the helical state becomes higher than that for the double-Q collinear ($2Q$ collinear) and $4Q$ CBL states for $I^z > 0$. Then, we show that the $4Q$ CBL state is chosen as the ground state by additionally considering the effect of the positive biquadratic interaction in Sec. III B. Lastly, we construct the magnetic-field phase diagram while changing the easy-axis two-spin anisotropic interaction (I^z) in Sec. III C.

A. Octuple-period spin density waves

First, let us consider the situation where the effect of the biquadratic interaction is negligible, i.e., $K = 0$; the model reduces to the RKKY model with the bilinear exchange interaction. By further considering the zero-field case $H = 0$, the magnetic instability at zero temperature is determined by the ratio of I^z/J. When $I^z = 0$, i.e., the isotropic case, the ground state is given by the single-Q spiral state with $\boldsymbol{Q}_\nu$, where the spiral plane is arbitrary.

Next, we introduce the easy-axis magnetic anisotropy by setting $I^z > 0$. By performing the simulated annealing in Sec. II, we find that two states with different spin configurations appear against I^z, as shown in Fig. 3(a): the $2Q$ collinear state and the $4Q$ CBL state. It is noted that these two states are energetically degenerate irrespective of the value of I^z, although their energy is lower than that in the single-Q spiral state. Thus, the multiple-Q instability occurs even without the biquadratic (multiple-spin) interaction or the magnetic field in the presence of an infinitesimally small I^z.

The real-space spin configurations and spin structure factors in the two states are shown in Figs. 3(b)–3(e). Both states are characterized by collinear spin textures, as shown in Fig. 3(b) for the $2Q$ collinear state and Fig. 3(c) for the $4Q$ CBL state. In other words, there are no xy-spin components in these two states. In the $2Q$ collinear state, the spin configuration is characterized by a double-Q superposition with different intensities at $\boldsymbol{Q}_1$ and $\boldsymbol{Q}_3$, as shown in the spin structure factor in Fig. 3(d). It is noteworthy that the constituent wave vectors in the $2Q$ collinear state are connected by the mirror symmetry rather than the rotational symmetry in contrast to conventional multiple-Q states including the SkL. Since these superpositions are not distinguishable from each other if the wave vectors are located at high-symmetric lines in the Brillouin zone like $\boldsymbol{Q}_\nu \parallel [100]$ or $\boldsymbol{Q}_\nu \parallel [110]$ [59], this result indicates that the low-symmetric ordering wave vectors can give rise to further intriguing multiple-Q states. A similar multiple-Q superposition also happens in the $4Q$ CBL state. In this case, a quadruple-Q superposition with equal intensities at $\boldsymbol{Q}_1$–$\boldsymbol{Q}_4$ appears in the spin structure factor so as to keep fourfold rotational symmetry, as shown in Fig. 3(e). Reflecting

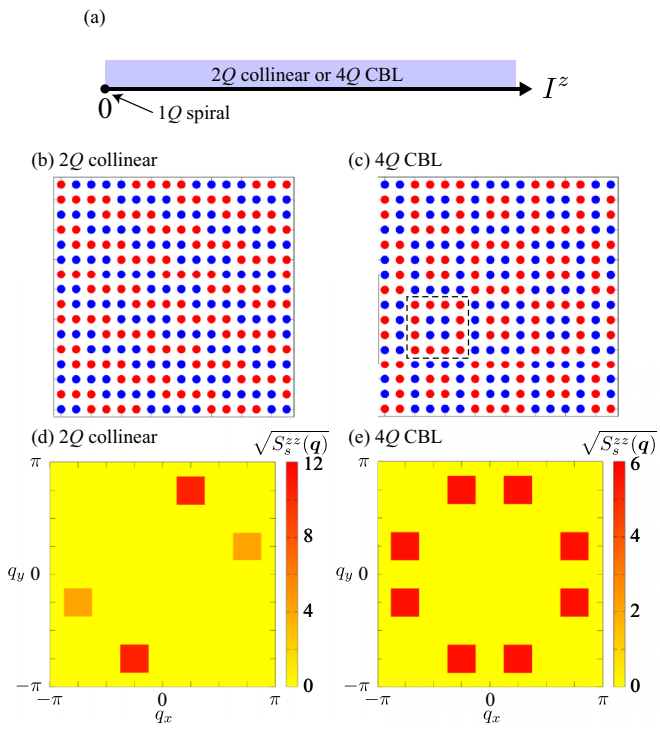

FIG. 3. (a) Ground-state phase diagram with changing I^z at $K = H = 0$. The $1Q$ spiral state only appears at $I^z = 0$; it degenerates with the $2Q$ collinear and $4Q$ CBL states. For $I^z > 0$, the $2Q$ collinear and $4Q$ CBL states become the ground state. Real-space spin configuration of (b) the $2Q$ collinear state and (c) the $4Q$ CBL state. The red and blue circles represent $S^z_i = +1$ and $S^z_i = -1$, respectively. In panel (c), the dashed square denotes the unit of the bubble. The z component of the spin structure factor of (d) the $2Q$ collinear state and (e) the $4Q$ CBL state.

the fourfold-symmetric spin structure factor, the real-space spin configuration is also fourfold-symmetric, as shown in Fig. 3(c). By closely looking at the real-space spin configuration, one finds that the unit of the bubble denoted by the dashed square aligns in a checkerboard way; the "antibubble" with the opposite S^z_i to the bubble appears next to the bubble so that the total magnetization in the whole system vanishes. This is why we call this state the $4Q$ CBL state.

We find the analytical expressions of the spin configuration in these two states. In the $2Q$ collinear state, it is given by

$$S^z_i = \frac{1}{\sqrt{2}}\Big[-\sin\Big(\boldsymbol{Q}_1\cdot\boldsymbol{r}_i - \frac{\pi}{4}\Big) - \sin(\boldsymbol{Q}_1\cdot\boldsymbol{r}_i) + \sin\Big(\boldsymbol{Q}_3\cdot\boldsymbol{r}_i + \frac{\pi}{4}\Big) - \sin(\boldsymbol{Q}_3\cdot\boldsymbol{r}_i)\Big], \tag{7}$$

with $S^x_i = S^y_i = 0$. Meanwhile, the spin pattern in the $4Q$ CBL state is given by

$$S^z_i = \frac{1}{\sqrt{2}}\Big[\sin\Big(\boldsymbol{Q}_1\cdot\boldsymbol{r}_i + \frac{\pi}{4}\Big) + \sin(\boldsymbol{Q}_2\cdot\boldsymbol{r}_i) - \sin\Big(\boldsymbol{Q}_3\cdot\boldsymbol{r}_i - \frac{\pi}{4}\Big) - \sin(\boldsymbol{Q}_4\cdot\boldsymbol{r}_i)\Big], \tag{8}$$

with $S^x_i = S^y_i = 0$. It is noted that both spin configurations in Eqs. (7) and (8) satisfy $|\boldsymbol{S}_i| = 1$ at any site without the normalization factor.

From the expressions in Eqs. (7) and (8), one obtains the $\boldsymbol{Q}_\nu$ component of the magnetic moments. In the $2Q$ collinear state, nonzero $(m^z_{\boldsymbol{Q}_\nu})^2$ are given by

$$\big(m^z_{\boldsymbol{Q}_1}\big)^2 = \frac{2+\sqrt{2}}{8}, \quad \big(m^z_{\boldsymbol{Q}_3}\big)^2 = \frac{2-\sqrt{2}}{8}, \tag{9}$$

and, in the $4Q$ CBL state, they are given by

$$\big(m^z_{\boldsymbol{Q}_1}\big)^2 = \big(m^z_{\boldsymbol{Q}_2}\big)^2 = \big(m^z_{\boldsymbol{Q}_3}\big)^2 = \big(m^z_{\boldsymbol{Q}_4}\big)^2 = \tfrac{1}{8}. \tag{10}$$

From the relation $(m_{-\boldsymbol{Q}_\nu})^2 = (m_{\boldsymbol{Q}_\nu})^2$, both states satisfy $\sum_\nu[(m^z_{\boldsymbol{Q}_\nu})^2 + (m^z_{-\boldsymbol{Q}_\nu})^2] = 1$, which indicates that there are no contributions from the magnetic moments with the high-harmonic wave vectors.

It is surprising that no intensities at high-harmonic wave vectors appear in both the $2Q$ collinear and $4Q$ CBL states in spite of their multiple-Q structures. Although similar situations have been found when the multiple-Q wave vectors lie at the high-symmetric points at the Brillouin zone boundary [61,74,75], the case under the low-symmetric ordering wave vectors is rare [76]; for example, the double-Q SkL consisting of the wave vectors $\boldsymbol{q}_1$ and $\boldsymbol{q}_2$ with $\boldsymbol{q}_1 \perp \boldsymbol{q}_2$ exhibits the intensity at $\boldsymbol{q}_1 + \boldsymbol{q}_2$ [77].

The absence of high-harmonic wave-vector contributions is understood from the geometry and symmetry of the constituent ordering wave vectors $\boldsymbol{Q}_1$–$\boldsymbol{Q}_4$. When considering the sinusoidal spiral modulation at the $\boldsymbol{Q}_1$ component, the high-harmonic wave vectors contributing to the spin configuration are attributed to $3\boldsymbol{Q}_1, 5\boldsymbol{Q}_1, 7\boldsymbol{Q}_1, \ldots$ owing to the local constraint of the spin length ($|\boldsymbol{S}_i| = 1$). In the present choice of $\boldsymbol{Q}_1 = (\pi/4, 3\pi/4)$, these high-harmonic wave vectors are reduced to the symmetry-equivalent ones to $\boldsymbol{Q}_1$ except for the translation by the reciprocal lattice vectors $\boldsymbol{G}_1 = (2\pi, 0)$ and $\boldsymbol{G}_2 = (0, 2\pi)$ as follows:

$$\begin{aligned} 3\boldsymbol{Q}_1 &= \Big(\frac{3\pi}{4}, \frac{9\pi}{4}\Big) = \boldsymbol{Q}_3\delta_{\boldsymbol{G}_2,\boldsymbol{0}}, \\ 5\boldsymbol{Q}_1 &= \Big(\frac{5\pi}{4}, \frac{15\pi}{4}\Big) = -\boldsymbol{Q}_3\delta_{\boldsymbol{G}_1,\boldsymbol{0}}\delta_{\boldsymbol{G}_2,\boldsymbol{0}}, \\ 7\boldsymbol{Q}_1 &= \Big(\frac{7\pi}{4}, \frac{21\pi}{4}\Big) = -\boldsymbol{Q}_1\delta_{\boldsymbol{G}_1,\boldsymbol{0}}\delta_{\boldsymbol{G}_2,\boldsymbol{0}}, \\ 9\boldsymbol{Q}_1 &= \Big(\frac{9\pi}{4}, \frac{27\pi}{4}\Big) = \boldsymbol{Q}_1\delta_{\boldsymbol{G}_1,\boldsymbol{0}}\delta_{\boldsymbol{G}_2,\boldsymbol{0}}, \end{aligned} \tag{11}$$

where δ is the Kronecker delta; see also Fig. 4. This result indicates that the relation of the octuple-period wave vectors connected by the mirror symmetry is essential, which is characteristic of the low-symmetric wave vectors. Similarly, $3\boldsymbol{Q}_2, 5\boldsymbol{Q}_2, 7\boldsymbol{Q}_2, \ldots$ are described by $\pm\boldsymbol{Q}_2$ and $\pm\boldsymbol{Q}_4$. This is why these multiple-Q states have the intensities only at $\boldsymbol{Q}_1$, $\boldsymbol{Q}_2$, $\boldsymbol{Q}_3$, and $\boldsymbol{Q}_4$. Such a situation does not hold for high-symmetric wave vectors along the [100] and [110] directions and other low-symmetric wave vectors except for

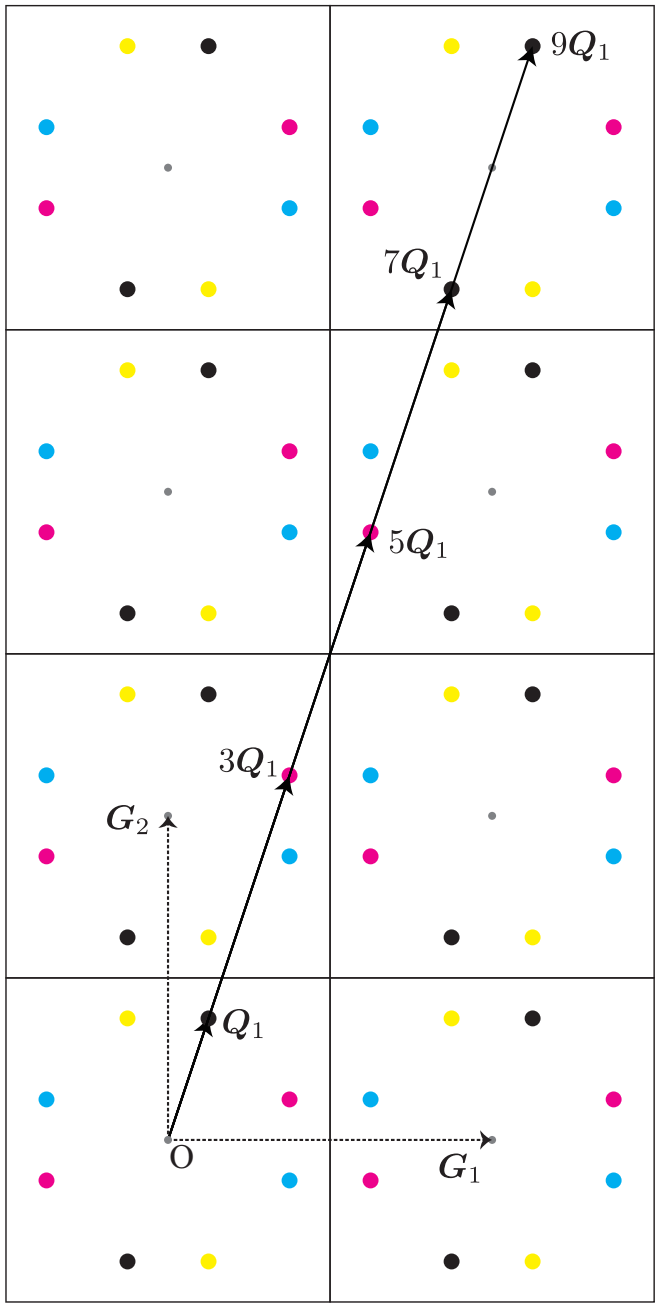

FIG. 4. Ordering wave vectors at $\boldsymbol{Q}_1$, $3\boldsymbol{Q}_1$, $5\boldsymbol{Q}_1$, $7\boldsymbol{Q}_1$, and $9\boldsymbol{Q}_1$ in the extended Brillouin zone. $\boldsymbol{G}_1$ and $\boldsymbol{G}_2$ represent the reciprocal lattice vectors.

octuple-period ones, such as $\boldsymbol{q} = (3\pi/4, 3\pi/8)$; the single-$Q$ spiral state is favored instead of multiple-Q states irrespective of the presence or absence of I^z. In other words, the octuple-period ordering wave vectors play an important role. We discuss the results for the different ordering wave vectors from $\boldsymbol{Q}_1$–$\boldsymbol{Q}_4$ in Appendix A.

The expressions in Eqs. (7) and (8) also mean degenerate energies between the $2Q$ collinear and $4Q$ CBL states. By calculating the energy from the Hamiltonian in Eq. (2), it is given by $J(1 + I^z)$ for both states. Thus, these states have the same energy within the bilinear RKKY interaction, which indicates that other interactions, such as higher-order interactions, are required to lift their degeneracy, as is discussed in the next section.

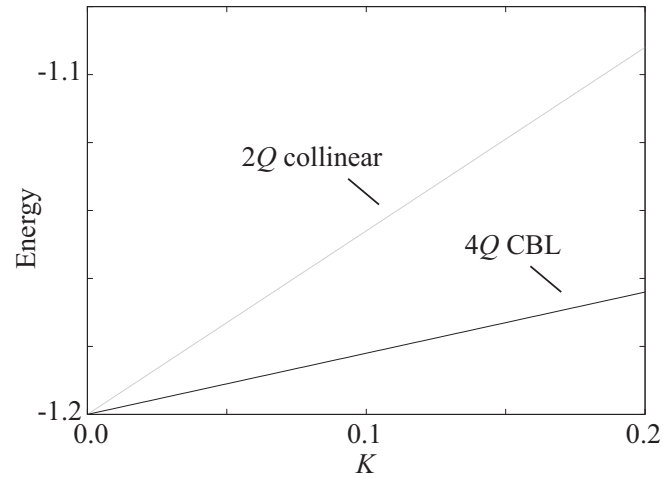

FIG. 5. K dependence of the energy in the $2Q$ collinear and $4Q$ CBL states at $I^z = 0.2$ and $H = 0$.

B. Instability toward checkerboard bubble lattice

To lift the degeneracy within the RKKY interaction, let us consider the effect of the biquadratic interaction K. We show the K dependence of the energy for the $2Q$ collinear and $4Q$ CBL states at $I^z = 0.2$ and $H = 0$ in Fig. 5. The data clearly show that their degeneracy is lifted for an infinitesimal small K; the energy in the $4Q$ CBL state becomes lower (higher) than that in the $2Q$ collinear state for $K > 0$ ($K < 0$). This is also understood from the expressions in Eqs. (7) and (8): the energy cost by K in the $2Q$ collinear state is evaluated as $3K(1 + I^z)^2/8$, while that in the $4Q$ CBL state is evaluated as $K(1 + I^z)^2/8$. Thus, nonzero positive (negative) K leads to instability toward the $4Q$ CBL ($2Q$ collinear) state.

C. Phase diagram under external magnetic field

We construct the magnetic phase diagram under the external magnetic field at $K = 0.05$ in Fig. 6. As shown in the phase diagram, the $4Q$ CBL state is stabilized in the low-field region irrespective of I^z, as discussed in Sec. III B. As H is increased, the $4Q$ CBL state turns into another quadruple-Q ($4Q$) state, whose real-space spin configuration and spin structure factor are shown in Fig. 7. We also plot the H dependence of M^z, $(m^{xy}_{\boldsymbol{Q}_\nu})^2$, and $(m^{z}_{\boldsymbol{Q}_\nu})^2$ at several I^z in Fig. 8.

As shown in the real-space spin configuration in Fig. 7(a) for $H = 1$ and Fig. 7(b) for $H = 1.5$, the $4Q$ state exhibits a complicated non-coplanar spin texture. Similarly to the $4Q$ CBL state, the $4Q$ state is characterized by the quadruple-Q peaks with the same intensity in the spin structure factor, although such a peak structure appears in the xy-spin component rather than the z-spin one, as shown in Figs. 7(c) and 7(d). Thus, this phase transition is regarded as a spin-flop transition, where the spin modulation changes from the z direction parallel to H to the xy plane perpendicular to H. It is noted that all the intensities in the spin structure factor are located at $\boldsymbol{Q}_\nu$ so that the contributions from other wave vectors are absent,

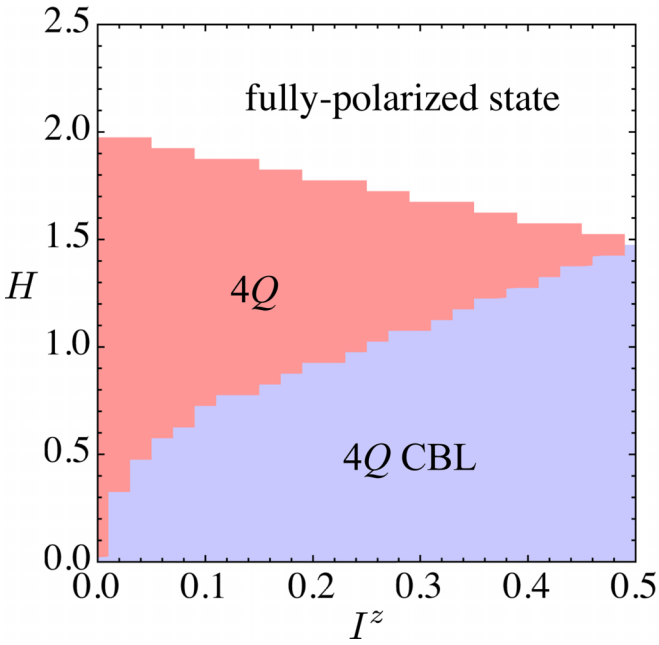

FIG. 6. Magnetic ground-state phase diagram in the plane of I^z and H at $K = 0.05$, which is obtained by the simulated annealing for the model in Eq. (2).

which might be attributed to the fact that the high-harmonic wave vectors, like $3\boldsymbol{Q}_1$, $5\boldsymbol{Q}_1$, $7\boldsymbol{Q}_1$, and so on, correspond to the symmetry-equivalent ones, as discussed in Sec. III A. It is also noted that there is no net scalar spin chirality in this state.

From the result in Fig. 8, the transition between the $4Q$ CBL and $4Q$ states is of first order with jumps of M^z, $(m^{xy}_{\boldsymbol{Q}_\nu})^2$, and $(m^{z}_{\boldsymbol{Q}_\nu})^2$ in Figs. 8(a) and 8(b). Especially, one finds the

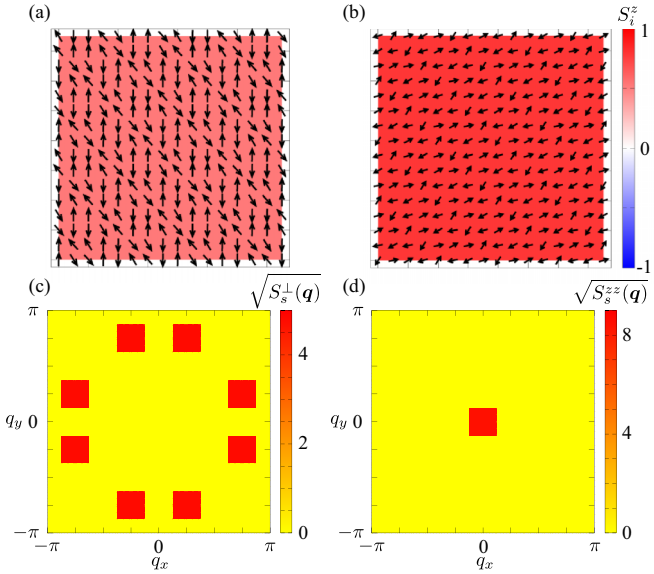

FIG. 7. Real-space spin configuration of the $4Q$ state in the high-field region for (a) $H = 1$ and (b) $H = 1.5$ at $I^z = 0.1$. The arrows and color denote the xy- and z-spin components, respectively. Square root of the spin structure factor in (c) the xy and (d) z components at $H = 1$ and $I^z = 0.1$.

magnetic plateau in the zero-field region, indicating a finite spin gap owing to the collinear spin configuration along the easy-axis direction. By further increasing H in the $4Q$ state, $(m^{xy}_{\boldsymbol{Q}_\nu})^2$ is gradually reduced and this state continuously changes into the fully polarized state with $S_i^z = 1$.

When I^z is increased, the region of the $4Q$ state is shrunk and vanishes at $I^z = 0.5$; the direct transition from the $4Q$ CBL state to the fully polarized state occurs by a drastic jump of the magnetization from $M^z = 0$ to $M^z = 1$, as shown in Fig. 8(c). The critical value of H between this direct transition is given by $|-J(1+I^z)+K(1+I^z)^2/8|$.

IV. DISCUSSION

A. Charge density wave

Since the $4Q$ CBL state exhibits no intensity at high-harmonic wave vectors, such as $\boldsymbol{Q}_1 + \boldsymbol{Q}_2$, it is difficult to distinguish the $4Q$ CBL state from the multidomain single-Q state or the multidomain $2Q$ collinear state in diffraction experiments, such as the small-angle neutron scattering, in contrast to the conventional multiple-Q states like the SkL. We here propose how to identify the $4Q$ CBL state by other measurements. One of the powerful measurements is the spectroscopic-imaging scanning tunneling microscopy measurement, which has been recently used to detect multiple-Q states in $GdRu_2Si_2$ [53]. This method enables us to derive the charge density modulations in real and momentum spaces, which are brought about by the formation of magnetic textures [78].

As an example, we show the charge-density distributions in the $2Q$ collinear state and the $4Q$ CBL state in both real and momentum spaces in Figs. 9(a) and 9(b), respectively. Here, we calculate these quantities for the original Kondo lattice model, which is given by

$$\mathcal{H} = -t \sum_{i,j,\sigma} c^{\dagger}_{i\sigma} c_{j\sigma} + J_{\rm K} \sum_{i} \boldsymbol{s}_i \cdot \boldsymbol{S}_i, \tag{12}$$

where $c^{\dagger}_{i\sigma}$ and $c_{i\sigma}$ are creation and annihilation operators of an itinerant electron at site i and spin σ. For simplicity, we consider the nearest-neighbor hopping $t = 1$ in the first term and we set $J_{\rm K} = 0.2$; $\boldsymbol{s}_i$ is the itinerant electron spin and $\boldsymbol{S}_i$ is the localized spins. For $\boldsymbol{S}_i$, we substitute the expressions in Eqs. (7) or (8). The local charge density measured from the average density is given by $n_i = \sum_\sigma \langle c^{\dagger}_{i\sigma} c_{i\sigma} \rangle - n^{\rm ave}$ ($n^{\rm ave}$ is the average density) and the charge structure factor is given by

$$n(\boldsymbol{q}) = \frac{1}{N} \sum_{ij} n_i n_j e^{i\boldsymbol{q}\cdot(\boldsymbol{r}_i - \boldsymbol{r}_j)}. \tag{13}$$

We set the chemical potential $\mu = 0.5$ without loss of generality.

As shown by the real-space charge distributions in the left panels of Figs. 9(a) and 9(b), both $2Q$ collinear and $4Q$ CBL states accompany charge modulations but their spatial alignments are different from each other; the modulated pattern breaks the fourfold rotational symmetry for the $2Q$ collinear state, while it keeps the fourfold rotational symmetry for the $4Q$ CBL state. Such a feature is clearly seen in momentum space, as shown in the right panels of Figs. 9(a) and 9(b). The $2Q$ collinear state exhibits the intensity at

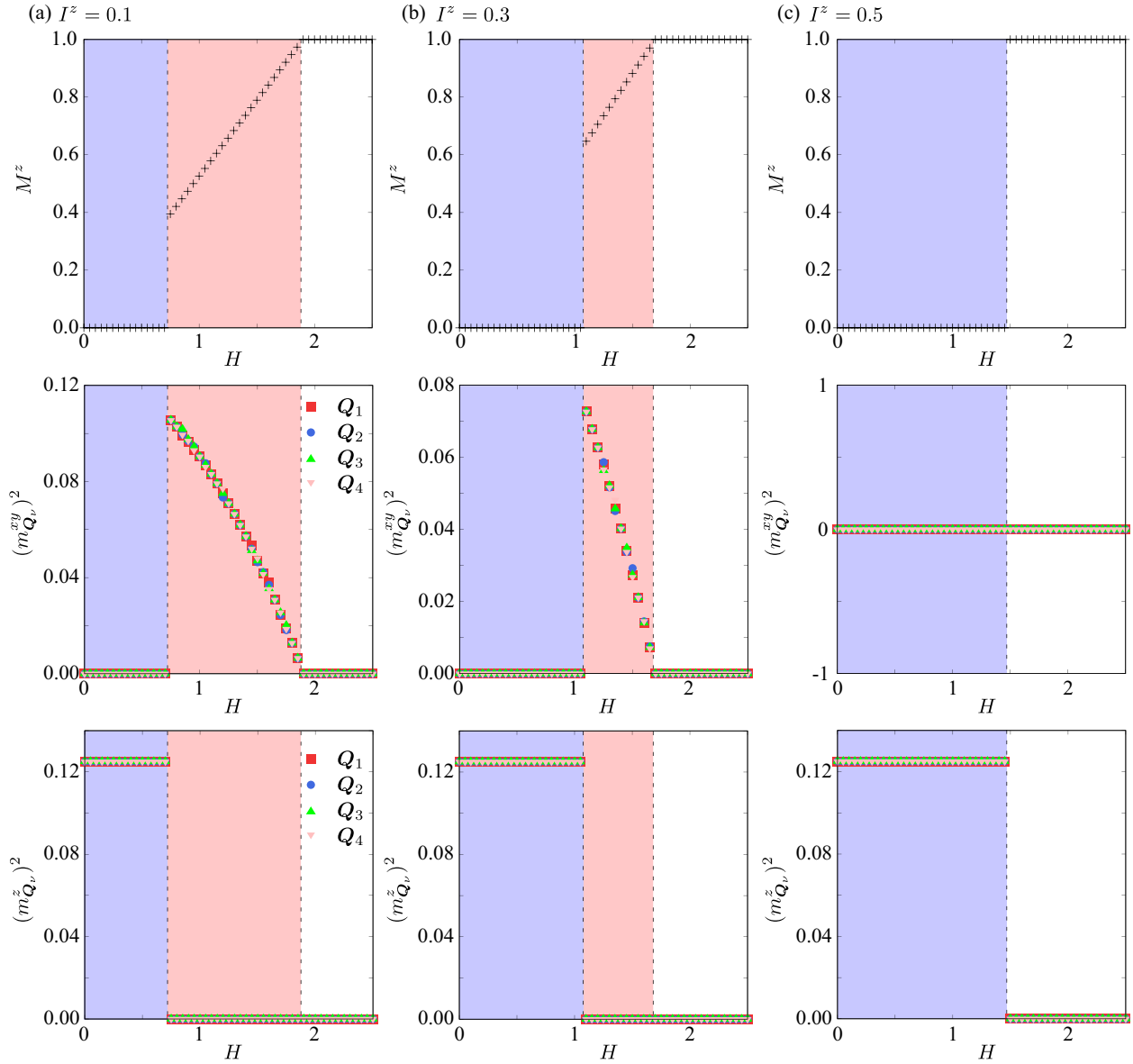

FIG. 8. H dependence of the magnetization M^z (top panels), $(m^{xy}_{\boldsymbol{Q}_\nu})^2$ (middle panels), and $(m^{z}_{\boldsymbol{Q}_\nu})^2$ (bottom panels) for (a) $I^z = 0.1$, (b) $I^z = 0.3$, and (c) $I^z = 0.5$ at $K = 0.05$. The vertical lines represent the phase boundaries between different magnetic states.

$\boldsymbol{Q}^{\rm CDW}_{2Q} = (-\pi/2, \pi/2)$, while the $4Q$ CBL state exhibits the intensities at $\boldsymbol{Q}^{\rm CDW}_{4Q} = (-\pi/2, \pi/2)$, $\boldsymbol{Q}'^{\rm CDW}_{4Q} = (\pi/2, \pi/2)$, $\boldsymbol{Q}''^{\rm CDW}_{4Q} = (\pi/2, 0)$, and $\boldsymbol{Q}'''^{\rm CDW}_{4Q} = (0, \pi/2)$.

The emergent peak positions in the charge structure factor are analytically derived from the expression as [78]

$$n_{\boldsymbol{q}} \propto \sum_{\boldsymbol{q}_1, \boldsymbol{q}_2} (\boldsymbol{S}_{\boldsymbol{q}_1} \cdot \boldsymbol{S}_{\boldsymbol{q}_2}) \delta_{\boldsymbol{q}_1+\boldsymbol{q}_2, \boldsymbol{q}+l_1\boldsymbol{G}_1+l_2\boldsymbol{G}_2}, \tag{14}$$

where $n_{\boldsymbol{q}}$ is the Fourier transform of n_i and $l_{1,2}$ are integers. By substituting the expression in Eq. (7) into $(\boldsymbol{S}_{\boldsymbol{q}_1} \cdot \boldsymbol{S}_{\boldsymbol{q}_2})$ in Eq. (14), one finds that $n_{\boldsymbol{Q}_1+\boldsymbol{Q}_3} = 0$ but $n_{\boldsymbol{Q}_1-\boldsymbol{Q}_3} \neq 0$ and $n_{2\boldsymbol{Q}_3} \neq 0$ in the $2Q$ collinear state by using the relation $(-\pi/2, \pi/2) = \boldsymbol{Q}_1 - \boldsymbol{Q}_3 = 2\boldsymbol{Q}_3 - \boldsymbol{G}_1$. When the spin pattern of the $2Q$ collinear state is characterized by a superposition of the $\boldsymbol{Q}_2$ and $\boldsymbol{Q}_4$ components instead of the $\boldsymbol{Q}_1$ and $\boldsymbol{Q}_3$ ones, the charge modulation occurs at the $\boldsymbol{Q}_2 + \boldsymbol{Q}_4 = (\pi/2, \pi/2)$ component. Thus, the multidomain structure in the $2Q$ collinear state exhibits the charge modulations at $\boldsymbol{q} = (-\pi/2, \pi/2)$ and $(\pi/2, \pi/2)$.

In a similar manner, the finite intensities at $\boldsymbol{Q}^{\rm CDW}_{4Q}$, $\boldsymbol{Q}'^{\rm CDW}_{4Q}$, $\boldsymbol{Q}''^{\rm CDW}_{4Q}$, and $\boldsymbol{Q}'''^{\rm CDW}_{4Q}$ are explained by nonzero $(\boldsymbol{S}_{\boldsymbol{q}_1} \cdot \boldsymbol{S}_{\boldsymbol{q}_2})$ for $\boldsymbol{q}_1, \boldsymbol{q}_2 = \boldsymbol{Q}_1, \boldsymbol{Q}_2, \boldsymbol{Q}_3, \boldsymbol{Q}_4$. It is noteworthy that the $4Q$ CBL state accompanies the charge density waves at $\boldsymbol{Q}''^{\rm CDW}_{4Q}$ and $\boldsymbol{Q}'''^{\rm CDW}_{4Q}$, which do not appear in the $2Q$ collinear state. The appearance of $\boldsymbol{Q}''^{\rm CDW}_{4Q}$ and $\boldsymbol{Q}'''^{\rm CDW}_{4Q}$ is attributed to nonzero contributions from a superposition of $\pm\boldsymbol{Q}_1$ and $\pm\boldsymbol{Q}_4$

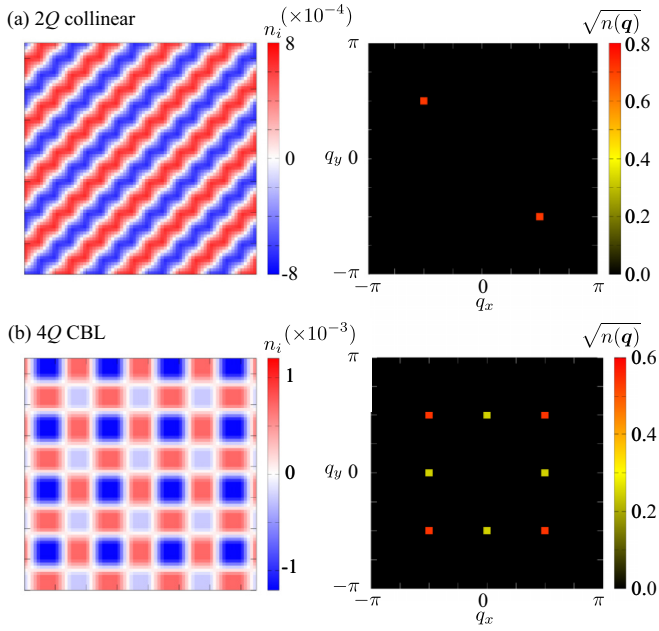

FIG. 9. (Left panels) Real-space distributions of the local charge density measured from the average density in (a) the $2Q$ collinear state and (b) the $4Q$ CBL state at $J_K = 0.2$ and $\mu = 0.5$. (Right panels) The square root of the charge structure factor except for the $\boldsymbol{q} = \boldsymbol{0}$ component.

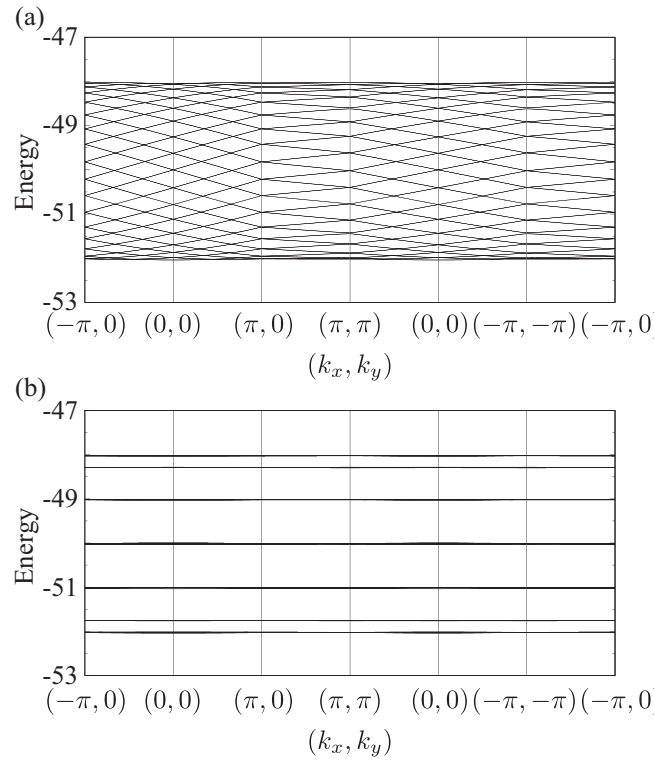

FIG. 10. Electronic band dispersion along the high-symmetric lines under (a) the $2Q$ collinear state and (b) the $4Q$ CBL state at $J_K = 100$.

($\pm\boldsymbol{Q}_3$ and $\pm\boldsymbol{Q}_2$), such as $\boldsymbol{Q}_1 - \boldsymbol{Q}_4 = (\pi/2, 0)$. Thus, the $2Q$ collinear and $4Q$ CBL states are distinguishable by detecting the charge density wave even in the presence of the multidomain structure.

B. Electronic band structure

Finally, let us discuss a characteristic electronic structure under the $4Q$ CBL state. By closely looking at the real-space spin configuration in Fig. 3(c), the down spins are surrounded by the up spins in the bubble denoted by the dashed square in the $4Q$ CBL state. This indicates the possibility of real-space localization when the itinerant electron spins are strongly coupled to localized spins, i.e., the double-exchange limit [79,80]. Indeed, one finds the nearly flat-band dispersion in the $4Q$ CBL state, while it does not appear in the $2Q$ collinear state, as shown in Figs. 10(b) and 10(a), in the strong-coupling regime; we set the lattice constant $a = 8$ in this section. We also show the electronic band structure far from the strong-coupling regime in the $4Q$ CBL state in Appendix B for reference. Thus, intriguing transport phenomena can be expected under the $4Q$ CBL state when the exchange coupling between itinerant electron spins and localized spins is strong.

V. SUMMARY

To summarize, we have investigated multiple-Q bubble-lattice instability consisting of sinusoidal spin density waves on the square lattice. By focusing on the geometry and symmetry of the ordering wave vectors in momentum space, we find that octuple-period spin density waves naturally give rise to two types of collinear multiple-Q superpositions, the $2Q$ collinear and $4Q$ CBL states, for an infinitesimal easy-axis magnetic anisotropy within the RKKY level. In contrast to conventional multiple-Q states consisting of spiral waves like the SkL, no intensities at high-harmonic wave vectors among the constituent ordering wave vectors appear in these states. We show that the $4Q$ CBL state becomes the ground state in

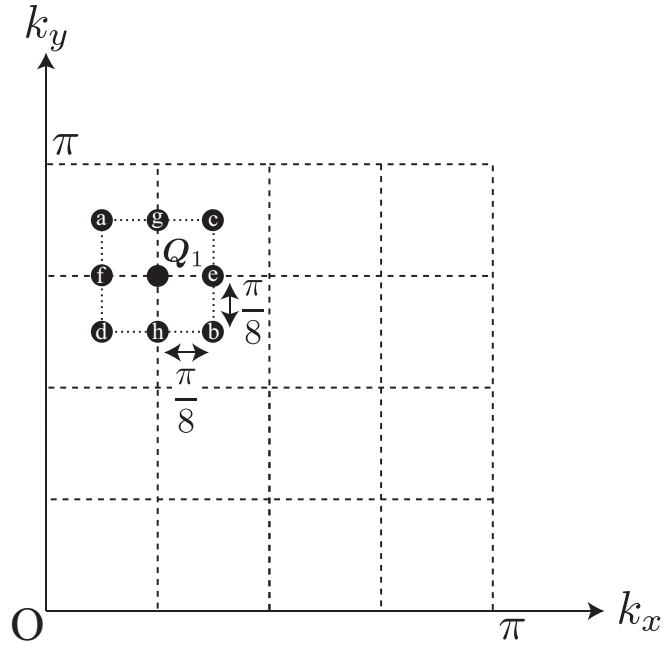

FIG. 11. The ordering vectors different from $\boldsymbol{Q}_1$.

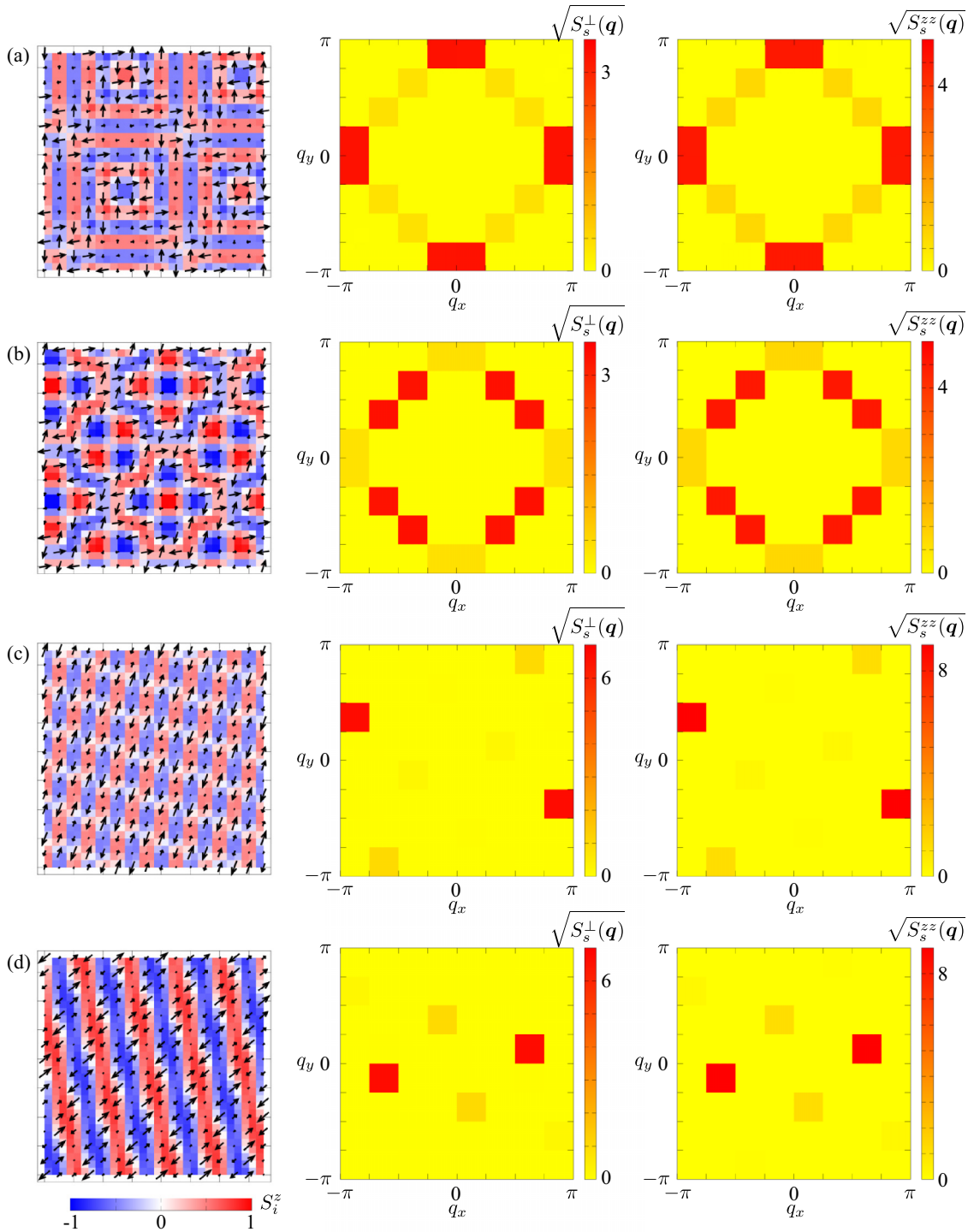

FIG. 12. (Left panels) Real-space spin configurations at $I^z = 0.2$, $K = 0.05$, and $H = 0$ for the ordering wave vectors (a) $\boldsymbol{Q}_a$, (b) $\boldsymbol{Q}_b$, (c) $\boldsymbol{Q}_c$, and (d) $\boldsymbol{Q}_d$. The arrows and color denote the xy- and z-spin components, respectively. (Middle and right panels) Square root of the spin structure factor in the xy and z components.

the presence of the positive biquadratic interaction by performing numerical and analytical calculations. In addition, we show that the 4Q CBL state exhibits the magnetization plateau in the zero-field region owing to the large spin gap. Moreover, we demonstrate that the 4Q CBL state accompanies the characteristic charge density waves, which are detected by the spectroscopic-imaging scanning tunneling microscopy measurements. We also discuss the nearly flat-band structure under the 4Q CBL state in the strong-coupling regime. Our results indicate a further possibility of realizing exotic multiple-Q states by controlling the positions of the ordering wave vectors.

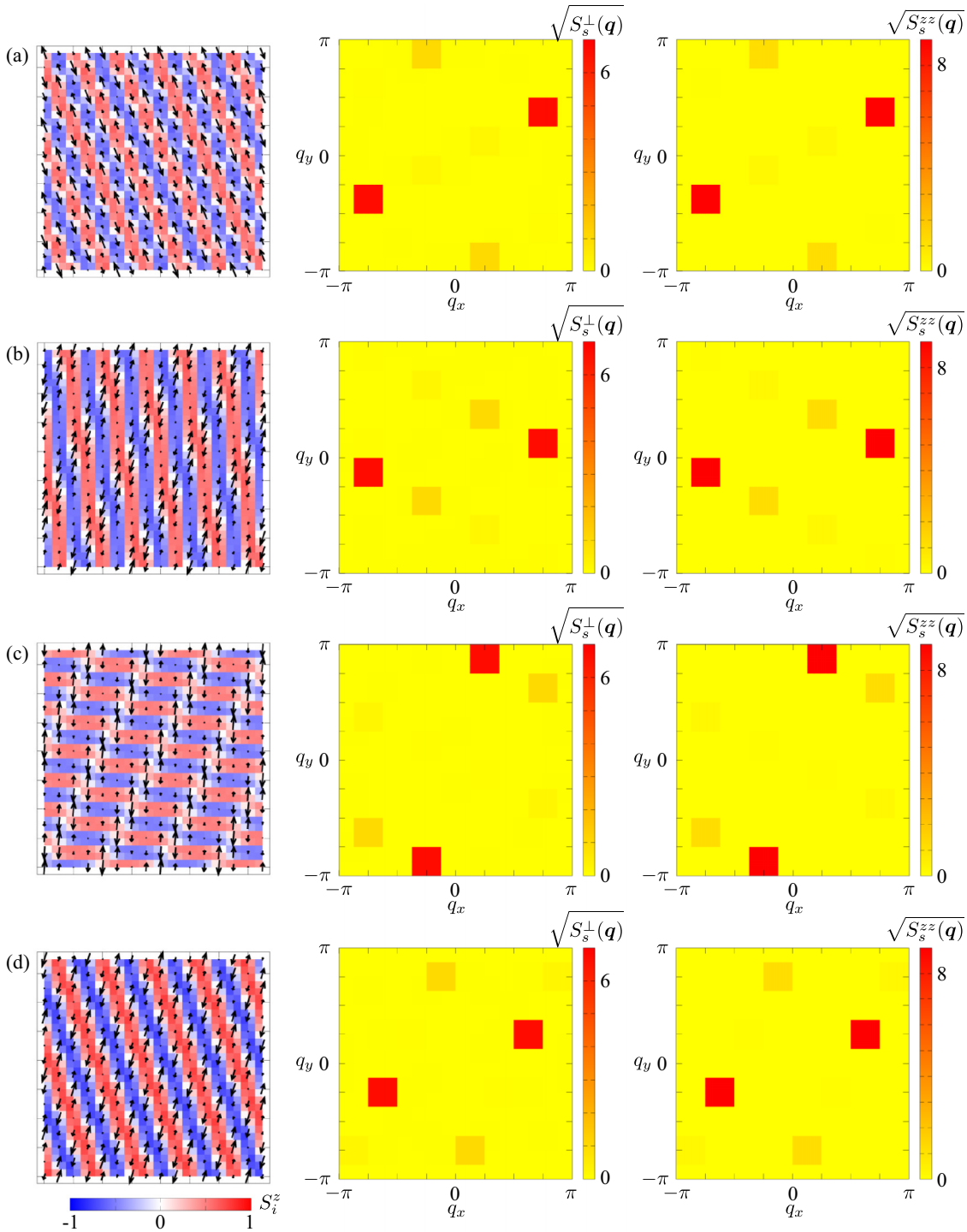

FIG. 13. The same plot as Fig. 12 for the different ordering wave vectors: (a) $\boldsymbol{Q}_e$, (b) $\boldsymbol{Q}_f$, (c) $\boldsymbol{Q}_g$, and (d) $\boldsymbol{Q}_h$.

ACKNOWLEDGMENTS

This research was supported by JSPS KAKENHI Grants No. JP21H01037, No. JP22H04468, No. JP22H00101, No. JP22H01183, No. JP23K03288, and No. JP23H04869 and by JST PRESTO (Grant No. JPMJPR20L8). Parts of the numerical calculations were performed on the supercomputing systems at the ISSP, the University of Tokyo.

APPENDIX A: SPIN CONFIGURATIONS FOR DIFFERENT ORDERING WAVE VECTORS

In this section, we investigate the instability toward multiple-Q states at the ordering wave vectors distinct from $\boldsymbol{Q}_1$ in the main text. We consider eight sets of the ordering wave vectors different from $\boldsymbol{Q}_1$, which are defined as

$$\boldsymbol{Q}_a = \boldsymbol{Q}_1 + \left(-\frac{\pi}{8}, \frac{\pi}{8}\right), \tag{A1}$$

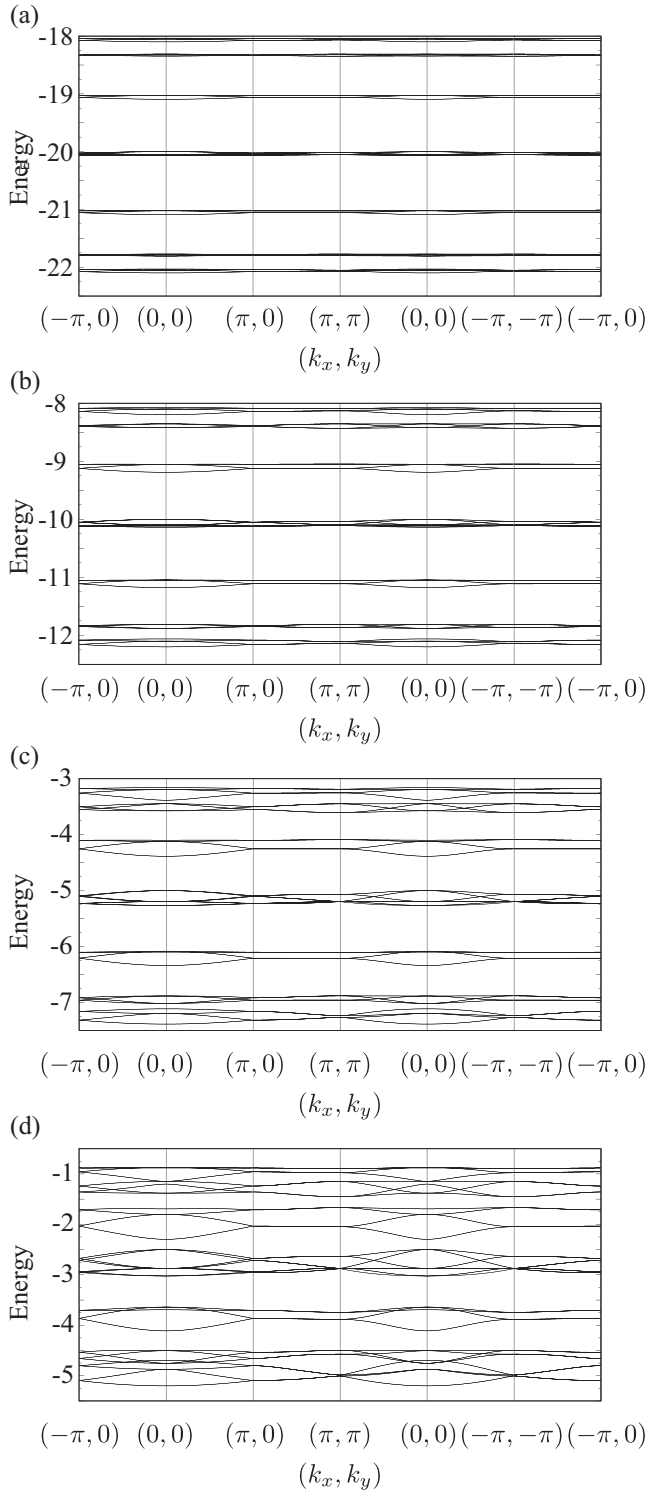

FIG. 14. Electronic band dispersion along the high-symmetric lines under the $4Q$ CBL state at (a) $J_{\rm K}=40$, (b) $J_{\rm K}=20$, (c) $J_{\rm K}=10$, and (d) $J_{\rm K}=5$.

$$\boldsymbol{Q}_b=\boldsymbol{Q}_1+\left(\frac{\pi}{8},-\frac{\pi}{8}\right), \tag{A2}$$

$$\boldsymbol{Q}_c=\boldsymbol{Q}_1+\left(\frac{\pi}{8},\frac{\pi}{8}\right), \tag{A3}$$

$$\boldsymbol{Q}_d=\boldsymbol{Q}_1+\left(-\frac{\pi}{8},-\frac{\pi}{8}\right), \tag{A4}$$

$$\boldsymbol{Q}_e=\boldsymbol{Q}_1+\left(\frac{\pi}{8},0\right), \tag{A5}$$

$$\boldsymbol{Q}_f=\boldsymbol{Q}_1+\left(-\frac{\pi}{8},0\right), \tag{A6}$$

$$\boldsymbol{Q}_g=\boldsymbol{Q}_1+\left(0,\frac{\pi}{8}\right), \tag{A7}$$

$$\boldsymbol{Q}_h=\boldsymbol{Q}_1+\left(0,-\frac{\pi}{8}\right), \tag{A8}$$

where we also change the positions of $\boldsymbol{Q}_2$–$\boldsymbol{Q}_4$ so that the fourfold rotational symmetry is satisfied. Figure 11 shows the positions of $\boldsymbol{Q}_a-\boldsymbol{Q}_h$.

By performing the simulated annealing for the model with the interactions at one out of eight ordering wave vectors in Eq. (A1)–(A8), we find that a similar multiple-Q instability appears for the cases with $\boldsymbol{Q}_a$ and $\boldsymbol{Q}_b$, while it does not for the cases with $\boldsymbol{Q}_c$–$\boldsymbol{Q}_h$. We show the data for the real-space spin configurations and spin structure factors at $I^z=0.2$, $K=0.05$, and $H=0$ in each case in Figs. 12(a)–12(d) and Figs. 13(a)–13(d); the quadruple-Q states with different spin configurations are realized in Figs. 12(a) and 12(b). From this observation, one finds that the ordering wave vectors lying on the line $Q^x+Q^y=\pi$ are important to induce the multiple-Q instability. Meanwhile, it is noted that the obtained quadruple-Q states have both xy- and z-spin components, which is different from the $4Q$ CBL state with the collinear spin texture in the main text. This difference is presumably owing to the different positions of the ordering wave vectors, which leads to the different superpositions of the spin density waves. Indeed, there are no intensities at wave vectors except for $\boldsymbol{Q}_1$–$\boldsymbol{Q}_4$ in the $4Q$ CBL state, while there are intensities at wave vectors distinct from $\boldsymbol{Q}_a$ ($\boldsymbol{Q}_b$) in the quadruple-Q state, as shown in the middle and right panels of Fig. 12(a) [Fig. 12(b)].

APPENDIX B: ELECTRONIC BAND STRUCTURES FAR FROM THE STRONG-COUPLING REGIME

We show the electronic band structure under the $4Q$ CBL spin texture for different values of $J_{\rm K}$ in Fig. 14. As shown in Fig. 14, the bands become more dispersive with decreasing $J_{\rm K}$, since the electrons can hop between the sites with antiparallel spins far from the double-exchange limit. Thus, the strong coupling is required to realize the flat-band structure, as discussed in Sec. IV B.

[1] U. K. Rößler, A. N. Bogdanov, and C. Pfleiderer, Nature (London) **442**, 797 (2006).

[2] S. Mühlbauer, B. Binz, F. Jonietz, C. Pfleiderer, A. Rosch, A. Neubauer, R. Georgii, and P. Böni, Science **323**, 915 (2009).

[3] X. Z. Yu, Y. Onose, N. Kanazawa, J. H. Park, J. H. Han, Y. Matsui, N. Nagaosa, and Y. Tokura, Nature (London) **465**, 901 (2010).

[4] X. Z. Yu, N. Kanazawa, Y. Onose, K. Kimoto, W. Zhang, S. Ishiwata, Y. Matsui, and Y. Tokura, Nat. Mater. **10**, 106 (2011).

[5] N. Nagaosa and Y. Tokura, Nat. Nanotechnol. **8**, 899 (2013).

[6] Y. Tokura and N. Kanazawa, Chem. Rev. **121**, 2857 (2021).

[7] S. D. Yi, S. Onoda, N. Nagaosa, and J. H. Han, Phys. Rev. B **80**, 054416 (2009).

[8] N. D. Khanh, T. Nakajima, X. Yu, S. Gao, K. Shibata, M. Hirschberger, Y. Yamasaki, H. Sagayama, H. Nakao, L. Peng *et al.*, Nat. Nanotechnol. **15**, 444 (2020).

[9] K. Karube, J. S. White, V. Ukleev, C. D. Dewhurst, R. Cubitt, A. Kikkawa, Y. Tokunaga, H. M. Rønnow, Y. Tokura, and Y. Taguchi, Phys. Rev. B **102**, 064408 (2020).

[10] N. D. Khanh, T. Nakajima, S. Hayami, S. Gao, Y. Yamasaki, H. Sagayama, H. Nakao, R. Takagi, Y. Motome, Y. Tokura *et al.*, Adv. Sci. **9**, 2105452 (2022).

[11] S. Seki, J.-H. Kim, D. S. Inosov, R. Georgii, B. Keimer, S. Ishiwata, and Y. Tokura, Phys. Rev. B **85**, 220406(R) (2012).

[12] S. Hayami and R. Yambe, Phys. Rev. B **107**, 174435 (2023).

[13] S. Ishiwata, M. Tokunaga, Y. Kaneko, D. Okuyama, Y. Tokunaga, S. Wakimoto, K. Kakurai, T. Arima, Y. Taguchi, and Y. Tokura, Phys. Rev. B **84**, 054427 (2011).

[14] T. Tanigaki, K. Shibata, N. Kanazawa, X. Yu, Y. Onose, H. S. Park, D. Shindo, and Y. Tokura, Nano Lett. **15**, 5438 (2015).

[15] N. Kanazawa, S. Seki, and Y. Tokura, Adv. Mater. **29**, 1603227 (2017).

[16] Y. Fujishiro, N. Kanazawa, T. Nakajima, X. Z. Yu, K. Ohishi, Y. Kawamura, K. Kakurai, T. Arima, H. Mitamura, A. Miyake *et al.*, Nat. Commun. **10**, 1059 (2019).

[17] S. Ishiwata, T. Nakajima, J.-H. Kim, D. S. Inosov, N. Kanazawa, J. S. White, J. L. Gavilano, R. Georgii, K. M. Seemann, G. Brandl *et al.*, Phys. Rev. B **101**, 134406 (2020).

[18] P. C. Rogge, R. J. Green, R. Sutarto, and S. J. May, Phys. Rev. Mater. **3**, 084404 (2019).

[19] Y. Kamiya and C. D. Batista, Phys. Rev. X **4**, 011023 (2014).

[20] C. Liu, R. Yu, and X. Wang, Phys. Rev. B **94**, 174424 (2016).

[21] L. Seabra, P. Sindzingre, T. Momoi, and N. Shannon, Phys. Rev. B **93**, 085132 (2016).

[22] S. Hayami, S.-Z. Lin, Y. Kamiya, and C. D. Batista, Phys. Rev. B **94**, 174420 (2016).

[23] G.-W. Chern, Y. Sizyuk, C. Price, and N. B. Perkins, Phys. Rev. B **95**, 144427 (2017).

[24] R. Takagi, J. White, S. Hayami, R. Arita, D. Honecker, H. Rønnow, Y. Tokura, and S. Seki, Sci. Adv. **4**, eaau3402 (2018).

[25] S. Hayami, T. Okubo, and Y. Motome, Nat. Commun. **12**, 6927 (2021).

[26] K. Kobayashi and S. Hayami, Phys. Rev. B **106**, L140406 (2022).

[27] M. Zhang, C. Wang, S. Dong, H. Zhang, Y. Han, and L. He, Phys. Rev. B **105**, 024411 (2022).

[28] T. Ishitobi and K. Hattori, Phys. Rev. B **107**, 104413 (2023).

[29] S. Hayami and Y. Motome, Phys. Rev. B **103**, 054422 (2021).

[30] D. Solenov, D. Mozyrsky, and I. Martin, Phys. Rev. Lett. **108**, 096403 (2012).

[31] R. Ozawa, S. Hayami, K. Barros, G.-W. Chern, Y. Motome, and C. D. Batista, J. Phys. Soc. Jpn. **85**, 103703 (2016).

[32] G. D. A. Wood, D. D. Khalyavin, D. A. Mayoh, J. Bouaziz, A. E. Hall, S. J. R. Holt, F. Orlandi, P. Manuel, S. Blügel, J. B. Staunton *et al.*, Phys. Rev. B **107**, L180402 (2023).

[33] B. Zager, R. Fan, P. Steadman, and K. Plumb, arXiv:2307.03776.

[34] T. Shimokawa and H. Kawamura, Phys. Rev. Lett. **123**, 057202 (2019).

[35] Y. Lin, P. Grundy, and E. Giess, Appl. Phys. Lett. **23**, 485 (1973).

[36] T. Garel and S. Doniach, Phys. Rev. B **26**, 325 (1982).

[37] S. Takao, J. Magn. Magn. Mater. **31-34**, 1009 (1983).

[38] T. Jungwirth, X. Marti, P. Wadley, and J. Wunderlich, Nat. Nanotechnol. **11**, 231 (2016).

[39] L. Caretta, M. Mann, F. Büttner, K. Ueda, B. Pfau, C. M. Günther, P. Hessing, A. Churikova, C. Klose, M. Schneider *et al.*, Nat. Nanotechnol. **13**, 1154 (2018).

[40] H. Callen and R. M. Josephs, J. Appl. Phys. **42**, 1977 (1971).

[41] F. De Leeuw, R. Van Den Doel, and U. Enz, Rep. Prog. Phys. **43**, 689 (1980).

[42] C. Moutafis, S. Komineas, and J. A. C. Bland, Phys. Rev. B **79**, 224429 (2009).

[43] Y. Xiao, F. Morvan, A. He, M. Wang, H. Luo, R. Jiao, W. Xia, G. Zhao, and J. Liu, Appl. Phys. Lett. **117**, 132402 (2020).

[44] M. Gutzeit, A. Kubetzka, S. Haldar, H. Pralow, M. A. Goerzen, R. Wiesendanger, S. Heinze, and K. von Bergmann, Nat. Commun. **13**, 5764 (2022).

[45] G. G. Marcus, D.-J. Kim, J. A. Tutmaher, J. A. Rodriguez-Rivera, J. O. Birk, C. Niedermeyer, H. Lee, Z. Fisk, and C. L. Broholm, Phys. Rev. Lett. **120**, 097201 (2018).

[46] J. Park, H. Sakai, A. P. Mackenzie, and C. W. Hicks, Phys. Rev. B **98**, 024426 (2018).

[47] S. Seo, X. Wang, S. M. Thomas, M. C. Rahn, D. Carmo, F. Ronning, E. D. Bauer, R. D. dos Reis, M. Janoschek, J. D. Thompson *et al.*, Phys. Rev. X **10**, 011035 (2020).

[48] S. Seo, S. Hayami, Y. Su, S. M. Thomas, F. Ronning, E. D. Bauer, J. D. Thompson, S.-Z. Lin, and P. F. Rosa, Commun. Phys. **4**, 58 (2021).

[49] S. Hayami, S.-Z. Lin, and C. D. Batista, Phys. Rev. B **93**, 184413 (2016).

[50] S. Hayami, J. Magn. Magn. Mater. **513**, 167181 (2020).

[51] S. Hayami and Y. Kato, Phys. Rev. B **108**, 024426 (2023).

[52] S. Hayami, New J. Phys. **23**, 113032 (2021).

[53] Y. Yasui, C. J. Butler, N. D. Khanh, S. Hayami, T. Nomoto, T. Hanaguri, Y. Motome, R. Arita, T. H. Arima, Y. Tokura *et al.*, Nat. Commun. **11**, 5925 (2020).

[54] S. Hayami and Y. Motome, J. Phys.: Condens. Matter **33**, 443001 (2021).

[55] S. Hayami, R. Ozawa, and Y. Motome, Phys. Rev. B **95**, 224424 (2017).

[56] M. A. Ruderman and C. Kittel, Phys. Rev. **96**, 99 (1954).

[57] T. Kasuya, Prog. Theor. Phys. **16**, 45 (1956).

[58] K. Yosida, Phys. Rev. **106**, 893 (1957).

[59] R. Yambe and S. Hayami, Phys. Rev. B **106**, 174437 (2022).

[60] Y. Akagi, M. Udagawa, and Y. Motome, Phys. Rev. Lett. **108**, 096401 (2012).

[61] S. Hayami and Y. Motome, Phys. Rev. B **90**, 060402(R) (2014).

[62] S. Hayami and Y. Motome, Phys. Rev. Lett. **121**, 137202 (2018).

[63] S. Hayami, J. Phys.: Condens. Matter **34**, 365802 (2022).

[64] S. Hayami and Y. Motome, Phys. Rev. B **103**, 024439 (2021).

[65] S. Hayami and Y. Kato, J. Magn. Magn. Mater. **571**, 170547 (2023).
[66] Z. Wang, Y. Su, S.-Z. Lin, and C. D. Batista, Phys. Rev. B **103**, 104408 (2021).
[67] S. Hayami, Phys. Rev. B **105**, 174437 (2022).
[68] O. I. Utesov, Phys. Rev. B **103**, 064414 (2021).
[69] S. Hayami, J. Phys. Soc. Jpn. **91**, 023705 (2022).
[70] S. Hayami and R. Yambe, Phys. Rev. B **105**, 104428 (2022).
[71] R. Takagi, N. Matsuyama, V. Ukleev, L. Yu, J. S. White, S. Francoual, J. R. L. Mardegan, S. Hayami, H. Saito, K. Kaneko *et al.*, Nat. Commun. **13**, 1472 (2022).
[72] S. Hayami, J. Phys. Mater. **6**, 014006 (2023).
[73] The present model with the exchange interactions at specific ordering wave vectors tends to avoid metastable states, such as multi-domain states, compared to the conventional model with the real-space exchange interactions.
[74] D. F. Agterberg and S. Yunoki, Phys. Rev. B **62**, 13816 (2000).
[75] I. Martin and C. D. Batista, Phys. Rev. Lett. **101**, 156402 (2008).
[76] S. Hayami, R. Ozawa, and Y. Motome, Phys. Rev. B **94**, 024424 (2016).
[77] S. Hayami and R. Yambe, J. Phys. Soc. Jpn. **89**, 103702 (2020).
[78] S. Hayami and Y. Motome, Phys. Rev. B **104**, 144404 (2021).
[79] C. Zener, Phys. Rev. **82**, 403 (1951).
[80] P. W. Anderson and H. Hasegawa, Phys. Rev. **100**, 675 (1955).